Supporting Information

Synthesis and Ultrafast Carrier Dynamics of Single-Crystal Two-Dimensional $CuInSe_2$ Nanosheets

Xin Tao, Elham Mafi, and Yi Gu

Department of Physics and Astronomy, Washington State University, Pullman, WA 99164

Absorption Spectrum of $CuInSe_2$ Nanosheets

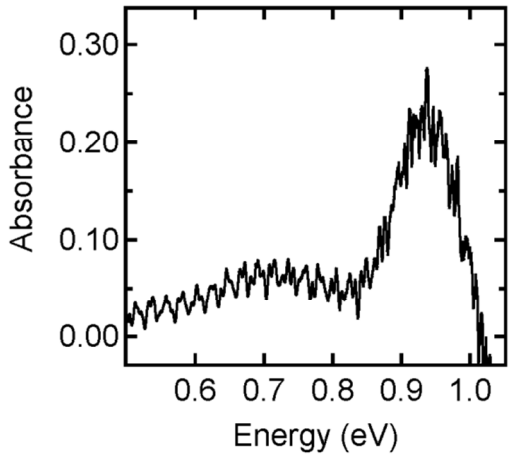

Figure S1 Absorbance spectrum of $CuInSe_2$ nanosheets.

We note that the absorption or the reflectivity measurements, while rather routine in typical thin film samples, are challenging in our case, because these $CuInSe_2$ nanosheets were obtained from exfoliated In_2Se_3 nanosheets, which have rather small areas (typically smaller than 10 × 10 μm) and are isolated from each other. Nonetheless, absorption or the reflectivity measurements are important to confirm the bandgap of the synthesized $CuInSe_2$ nanosheets. We therefore used van der Waals epitaxy-deposited In_2Se_3 thin nanosheets on mica substrates as the template for obtaining $CuInSe_2$ nanosheets. The synthesis procedures of In_2Se_3 thin nanosheets are similar to those reported in Lin *et al.*,.[S1] We note that, while we can obtain large-area and continuous $CuInSe_2$ nanosheets using this approach, the thickness of the $CuInSe_2$ nanosheets might be spatially non-uniform. Figure S1 shows an absorbance spectrum of $CuInSe_2$ nanosheets on a mica substrate that has been corrected for the absorption from the mica. This spectrum shows a bandgap energy of ~ 0.85 eV. We note that bandgap energies below 1 eV have been reported for

polycrystalline $CuInSe_2$ (Ref. S2). However, an accurate determination of the bandgap is difficult given the negative absorbance in the high energy region, which is an artificial effect resulting from the strong absorption from the mica.

Calculation of ΔR

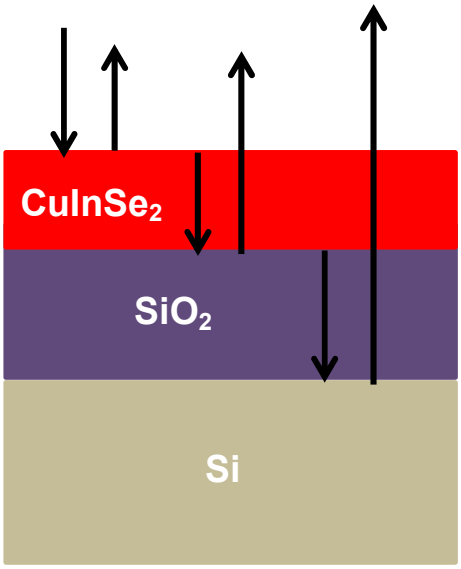

Figure S2 Schematic trilayer structure used to calculate ΔR. The beams are laterally shifted for clarity.

In the case of normal incidence of pump beam on a trilayer structure of $CuInSe_2$, SiO_2, and Si (Figure S2), the reflection coefficient of the system can be written as[S3]

$$R(n) = \left|\frac{r_1 e^{i(\Phi_1+\Phi_2)} + r_2 e^{-i(\Phi_1-\Phi_2)} + r_3 e^{-i(\Phi_1+\Phi_2)} + r_1 r_2 r_3 e^{i(\Phi_1-\Phi_2)}}{e^{i(\Phi_1+\Phi_2)} + r_1 r_2 e^{-i(\Phi_1-\Phi_2)} + r_1 r_3 e^{-i(\Phi_1+\Phi_2)} + r_2 r_3 e^{i(\Phi_1-\Phi_2)}}\right|^2$$

where

$$r_1 = \frac{\eta_0 - \eta_1}{\eta_0 + \eta_1},$$

$$r_2 = \frac{\eta_1 - \eta_2}{\eta_1 + \eta_2},$$

$$r_3 = \frac{\eta_2 - \eta_3}{\eta_2 + \eta_3},$$

$$\Phi_1 = \frac{2\pi d_1 \eta_1}{\lambda}$$

$$\Phi_2 = \frac{2\pi d_2 \eta_2}{\lambda}$$

η_0, η_1, η_2 and η_3 are the complex refraction indices of air, $CuInSe_2$, SiO_2, and Si, respectively, with $\eta = n - i(\alpha\lambda/4\pi)$, where n, α, and λ are the real refractive index, absorption coefficient, and the pump/probe wavelength. d_1 and d_2 are the thicknesses of $CuInSe_2$ and SiO_2, respectively, with λ as the wavelength of pump light. We chose a $CuInSe_2$ layer of thickness ~ 50 nm. The parameters used in the calculation are listed in Table S1. $\Delta R/R_0$ was calculated by varying n and α for $CuInSe_2$, with the results plotted in Figures 2 (c) and (d) in the main text.

Table S1 Parameters used to calculate ΔR

η_0	1
η_1	2.974-*i*0.763 (Ref. S4)
η_2	1.46
η_3	4.192-*i*0.036
d_1	50 nm
d_2	285 nm
λ	517 nm

Long-time Scans of -ΔR

Figure S3 shows the long-time decays of -ΔR plotted in a semi-logarithmic scale under various pump fluences. We note that, by using a large time-scan step (20 ps), which is larger than the time scale of the hot carrier cooling process, the contributions from hot carriers can be excluded and these decays are thus dominated by other relaxation dynamics. Particularly, as shown in the

figure, a fast component emerges as the pump fluence increases, whereas a slow component is present in all cases. Furthermore, the time constant of this fast component, obtained by single exponential fitting, decreases from ~ 441 ps to ~ 210 ps as the pump fluence increases. These behaviors indicate that this fast component is due to the Auger or the bimolecular recombination. It is difficult to differentiate between these two mechanisms, since the Auger process can also involve two particles (e.g. exciton-based interactions); however, this is beyond the scope of this work. On the other hand, the pump fluence has little effects on the slow component (with a time constant of ~ 1.1 ns), which might be due to rather low photogenerated carrier density following the preceding Auger or bimolecular recombinations. This slow component might be due to surface trap-assisted recombinations.

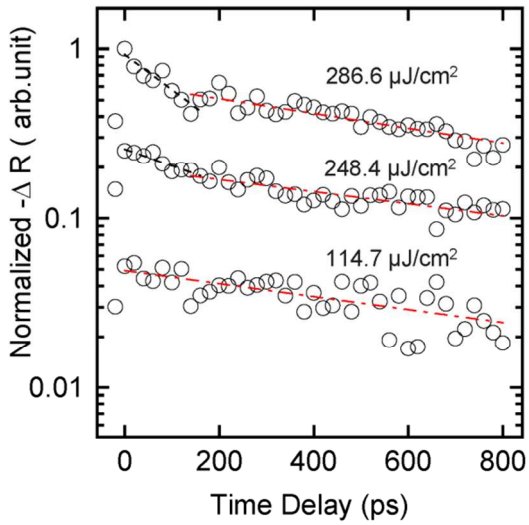

Figure S3 Long-time scans of normalized $-\Delta R$ (open circles) under various pump fluences, with dashed and dash-dotted lines representing single exponential fittings to the fast and slow decay components, respectively. Traces were vertically shifted for clarity.

Fitting Parameters for Figure 3 (a)

The equation of $-\Delta R = C_1 \times \exp(-t/\tau) + C_0$, where $C_{0,1}$ are constants and τ is the decay time, was used for fitting in Fig. 3 (a) in the main text. C_0 was used to account for the constant background (due to much slower decays at later time delays) that follows the initial fast decay of $-\Delta R$. Table S1 summaries the fitting parameters.

Table S2 Fitting Parameters for Figure 3 (a)

Pump Fluence (μJ/cm^2)	C_0	C_1	τ (ps)
143.3	17.594 ± 0.787	52.174 ± 3.79	0.41378 ± 0.0567
238.9	41.572 ± 0.897	65.129 ± 2.13	1.1873 ± 0.0828
286.6	57.965 ± 1.11	104.88 ± 2.36	1.3485 ± 0.0679

Deconvolution Procedures

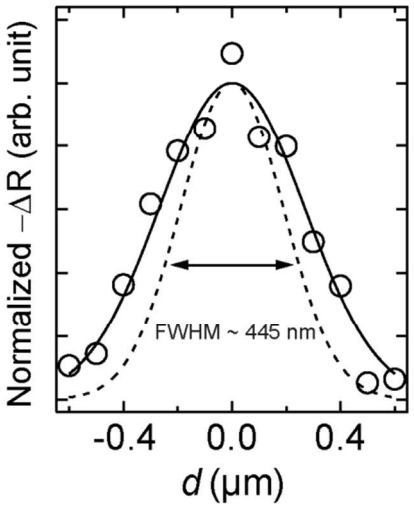

Figure S4 Profile of -Δ*R* (open circles) measured from a blank substrate fitted by a Gaussian function (solid line), with the dashed line as the deconvoluted probe beam profile with a FWHM of ~ 445 nm;

We assume that pump and probe beam profiles can be approximated by Gaussian distributions, and that pump and probe beams have the same spatial profile. With these assumptions, we measured -Δ*R* vs *d* on a blank substrate [open circles in Fig. S4], where there is no carrier diffusion. The measured -Δ*R* vs *d*, in this case, represents the convolution of two identical Gaussian functions (pump and probe beam profiles). A Gaussian function [solid line in Fig. S4]

was used to fit -Δ*R* vs *d*, and a subsequent simple Gaussian deconvolution procedure yields the probe beam profile, shown as the dashed line in Fig. S4, with a corresponding full-width-at-half-maximum (FWHM) of ~ 445 nm.

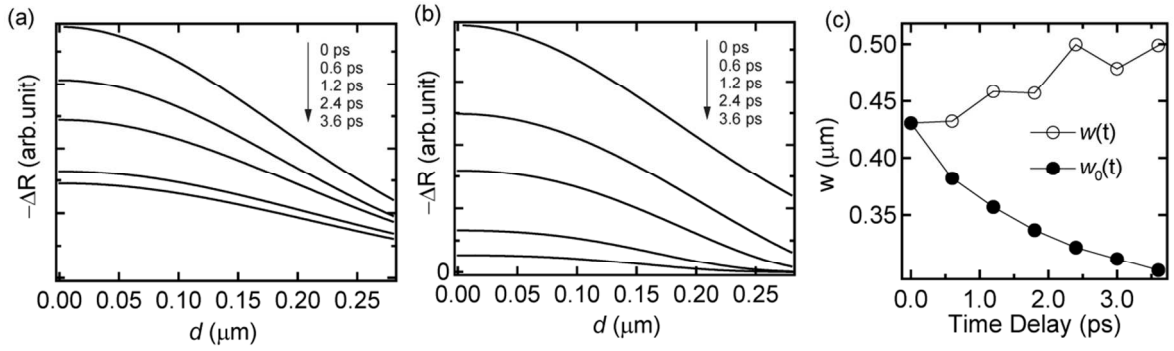

Figure S5 (a) Deconvoluted -Δ*R* vs *d* relations (Gaussian functions) obtained from the convoluted -Δ*R* vs *d* relations shown in Fig. 4 (a) in the main text; (b) calculated hot carrier spatial profile in the absence of carrier out-diffusion; (c) FWHM of calculated hot carrier spatial profile [w_0(t); solid circle-line] and of measured hot carrier spatial profile width after the deconvolution [*w*(t); open circle-line]

Similarly, the pump/probe beam profiles can also be obtained from -Δ*R* vs *d* measured on nanosheets at zero delay time [e.g. the top curve in Fig. 4 (a) in the main text], when no hot carrier diffusion has occurred. The FWHM of the pump/probe beam profiles measured using this approach varies to some extent across different samples, with an average value of ~ 410 nm, presumably due to the variations in the beam focusing condition for each measurement; nonetheless, these values are in reasonable agreement with that obtained on the blank substrate. For the deconvolution procedures applied to -Δ*R* vs *d* at later delay times, we used the probe beam profile measured at zero delay time on the same nanosheet for consistency of the beam focusing condition. We then fitted the plots of -Δ*R* vs *d* with Gaussian functions [e.g. dashed lines in Fig. 4 (a) in the main text] at various delay times. Next, the probe beam spatial profile was deconvoluted from these Gaussian functions. The results of deconvoluted -Δ*R* vs *d* relations

(Gaussian functions) are plotted in Figure S5 (a), with the corresponding FWHM values (open circles), *w*(t), plotted in Figure S5 (c).

Narrowing of the Hot Carrier Spatial Profile

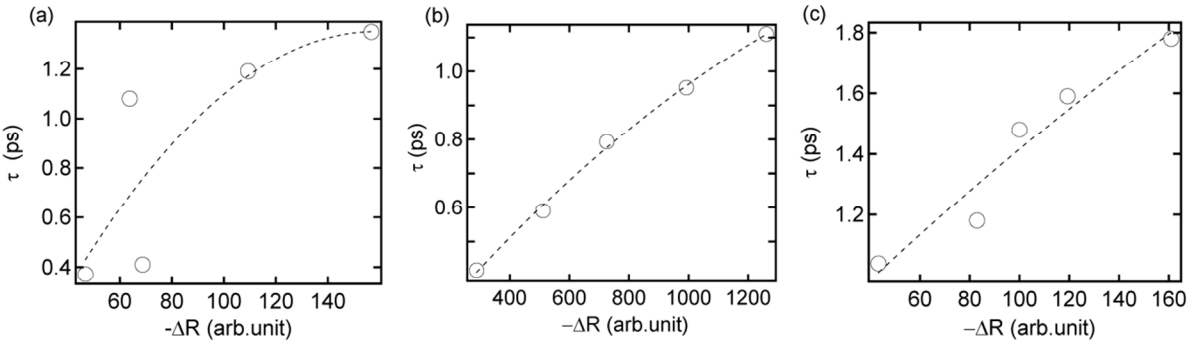

Figure S6 Hot carrier cooling time constants, τ (open circles), as a function of -Δ*R* (the value of which was measured at zero delay time for different pump fluences) obtained from three different nanosheets (a)-(c), with the dashed lines as the empirical polynomial fittings.

The hot carrier out-diffusion is not the only mechanism that leads to the change in *w*(t). Specifically, since the cooling of the hot carriers is slower when the hot carrier density is higher, the number of the hot carriers decays slower in the center of the pump beam spot, where the hot carrier density is higher, than in the regions away from the center. This mechanism alone would lead to a narrowing of the hot carrier spatial profile over time. To quantify this effect, we calculated the hot carrier spatial profiles, in the *absence* of the hot carrier diffusion. This calculation requires the knowledge of the hot carrier cooling time as a function of -Δ*R*, which can be obtained from the empirical polynomial fitting to the relation of τ vs -Δ*R*, with a few examples shown in Fig. S6 for different nanosheets. We note that the values of -Δ*R* were obtained at the zero time delay (i.e. at the peak of -Δ*R*) under different pump fluences. In other words, the τ vs -Δ*R* relations plotted here are reflective of the τ vs pump fluence relations. The results of the calculated hot carrier profiles, where there is no hot carrier out-diffusion, are

plotted in Fig. S5 (b), with the corresponding FWHM, $w_0(t)$, shown in Fig. S5 (c) as solid circles. $w_0(t)$, which decreases as the time progresses, represents the "baseline" for the determination of the hot carrier diffusion characteristics; particularly, $w(t) - w_0(t)$ is the width change due to the hot carrier out-diffusion.

References:

S1 Lin, M.; Wu, D.; Zhou, Y.; Huang, W.; Jiang, W.; Zheng, W. S.; Zhao, S. L.; Jin, C. H.; Guo, Y. F.; Peng, H. L., et al. Controlled Growth of Atomically Thin In_2Se_3 Flakes by Van Der Waals Epitaxy. *J. Am. Chem. Soc.* **2013,** *135*, 13274-13277.

S2 Sun, L. Y.; Kazmerski, L. L.; Clark, A. H.; Ireland, P. J.; Morton, D. W. Absorption Coefficient Measurement for Vacuum-Deposited Cu-Ternary Thin Films. J. Vac. Sci. Tech. **1978**, *15*, 265-268.

S3 Wang, R.; Ruzicka, B. A.; Kumar, N.; Bellus, M. Z.; Chiu, H. Y.; Zhao, H. Ultrafast and Spatially Resolved Studies of Charge Carriers in Atomically Thin Molybdenum Disulfide. *Phys Rev B* **2012,** *86*, 045406.

S4 Alonso, M.I.; Wakita, K.; Pascual, J. ; Garriga, M.; Yamamoto, N.. Optical Functions and Electronic Structure of $CuInSe_2$, $CuGaSe_2$, $CuInS_2$, and $CuGaS_2$. *Phys Rev B* **2001**, *63*, 075203.